Dalton Transactions

PAPER

View Article Online
View Journal | View Issue

Check for updates

Cite this: *Dalton Trans.*, 2019, **48**, 10547

Full-color emission of a Eu^{3+}-based mesoporous hybrid material modulated by Zn^{2+} ions: emission color changes for Zn^{2+} sensing *via* an ion exchange approach†

Zheng Zhang,‡ Heng Li,‡ Yajuan Li * and Xudong Yu

Received 20th April 2019,
Accepted 5th June 2019

DOI: 10.1039/c9dt01668f

rsc.li/dalton

We reported on the fabrication of a multicolor fluorescent sensor for Zn^{2+} ions based on the Eu complex functionalized mesoporous hybrid material Eu(TTA-MSN)$_2$L (TTA: 2-thenoyltrifluoroacetone, HL: 4′-(4-carboxy-methyleneoxyphenyl)-2,2′:6′,2″-terpyridinel). The material was characterized by Fourier transform infrared spectroscopy, X-ray diffraction, transmission electron microscopy, and N_2 adsorption measurements. The results revealed that the material preserves mesoscopically ordered structures and exhibited highly uniform pore size distributions. Spectroscopic analyses showed that the mesoporous hybrid material Eu(TTA-MSN)$_2$L exhibited the characteristic emission of Eu^{3+} ions, reasonably long lifetimes (0.62 ms), and high quantum yields (18.4%). Moreover, the material displayed a highly selective and sensitive function toward Zn^{2+} ions in aqueous solutions. This sensing function could be attributed to the cation exchange of Eu^{3+} in the parent material Eu(TTA-MSN)$_2$L with Zn^{2+}. More importantly, by only modulating the concentration of Zn^{2+} ions in the water solution of Eu(TTA-MSN)$_2$L, a tunable full-color emission (including white-light emission) can be generated under single-wavelength excitation. To our knowledge, this effort is the first example of a multicolor emissive sensor for Zn^{2+} ions in water solutions based on lanthanide mesoporous hybrid material.

Published on 05 June 2019. Downloaded by KEAN UNIVERSITY on 7/18/2019 2:41:27 AM.

Introduction

Multi-wavelength or multi-color luminescent materials, particularly those with white-light emission, have been extensively studied because of wide applications, including light-emitting diodes (LEDs), chemical sensing, bio-imaging, optoelectronic devices and displays.[1–6] Lanthanide-based luminescent materials are excellent candidates for designing multi-color and emitting materials due to their unique sharp emission bands, high fluorescence quantum efficiency, and long luminescence lifetimes. Jun Lin *et al.* recently demonstrated Tb^{3+}- and Mn^{2+}-codoped CCPO ($Ca_{19}Ce(PO_4)_{14}$) phosphors with abundant emission colors that were controlled by tunable energy transfer.[7] N. Holten-Andersen *et al.* developed multi-color emission (containing white-light emission) metallogels that contain lanthanide ions and display reversible stimuli-responsive properties.[8] However, to date, the generation of color- tunable rare earth-based materials has been dominated by controlling the stoichiometric ratios (level) of doped ions, and a blue light emission source should be introduced into the system when white emission color is achieved.[9–12] Processes with multiple components are complex and tedious. A simple method with fewer components to obtain the full-color emission particularly white emission color has yet to be established.

Zinc is the second-most abundant heavy metal ion in the human body, and it exists exclusively in its divalent form within biological environments. Zinc is an essential component of many enzymes, and it also plays critical roles in maintaining key structural features of genes.[13,14] Moreover, zinc ions participate in various biological activities, including neural-signal transmission, insulin secretion, and metalloenzyme regulation, as well as those that occur in the course of certain diseases, such as Alzheimer' s disease, infantile diarrhea, and diabetes. Therefore, the selective detection or sensing of Zn^{2+} is of great importance.[15–17] In the past decades, several Zn^{2+} fluorescent sensors based on lanthanide complex materials have been reported.[14,18,19] However, the poor photothermal and thermodynamic stabilities as well as the low mechanical strength of these probes restrict their practical applications to a large extent. One solution to overcome

College of Science, and Hebei Research Center of Pharmaceutical and Chemical Engineering, Hebei University of Science and Technology, Yuhua Road 70, Shijiazhuang 050080, PR China. E-mail: liyajuan0820@163.com; Fax: +86-311-81668548; Tel: +86-311-81668532

†Electronic supplementary information (ESI) available. See DOI: 10.1039/c9dt01668f

‡Joint first authors contributed equally to this work.

Published on 05 June 2019. Downloaded by KEAN UNIVERSITY on 7/18/2019 2:41:27 AM.

this drawback is to immobilize lanthanide complexes into stable rigid matrices, such as polymers, liquid crystals, or silica-based materials.[20–23] Among these matrices, mesoporous silica nanoparticles (MSNs) have gained considerable attention as supports for lanthanide complexes because they offer many novel and unique properties, such as large surface area, adjustable pore size, photostability, and easy recyclability. These characteristics allow MSNs to be favorably used as fluorescent sensors for the highly sensitive detection of specific metal ions. In addition, the response of lanthanide complex-based sensors toward Zn^{2+} typically originates from the coordination interaction between Zn^{2+} cations and free coordinate sites of organic ligands in lanthanide complexes.[24,25] Recent studies showed that cation exchange is a powerful strategy for constructing ion sensors with signal amplification effects or tunable photoinduced emission spectra.[26,27] However, lanthanide complex-based sensors for Zn^{2+} based on cation exchange have rarely been reported.

Inspired by these concepts, we fabricated a Eu complex functionalized mesoporous hybrid material Eu(TTA-MSN)$_2$L *via* a sol–gel method, which displays distinct emission color changes for the efficient and fast sensing of Zn^{2+} ions. The emission color changed from red to pink, white, blue, and then to green, allowing a visual and quantitative Zn^{2+} ion sensing process that is based on the emission color rather than the intensity changes. Therefore, a full-color emission containing white-light emission can be obtained under one fixed excitation by modulating only the concentration of Zn^{2+} ions in water solutions of mesoporous hybrid material Eu(TTA-MSN)$_2$L. To the best of our knowledge, this effort is the first multicolor emissive sensor for Zn^{2+} ions in water solutions based on the lanthanide mesoporous hybrid material. This work offers a novel and simple approach for achieving full-color emissions triggered only by the level of guest species.

Experimental

Materials

3-(Triethoxysilyl)propylisocyanate (TEPIC, 96%), triblock copolymer poly (ethylene glyco)-*block*-poly(propylene glycol)-*block*-poly-(ethylene glycol) (Pluronic P123, $EO_{20}PO_{70}EO_{20}$), 2-thenoyltrifluoroacetone (TTA, 99%), tetraethoxysilane (TEOS, A.R.), and sodium hydride (60%, dispersed in paraffin oil) were purchased from J&K Scientific Ltd. Eu$(NO_3)_3{\cdot}6H_2O$ was obtained by dissolving Eu_2O_3 (99.99%, J&K Scientific Ltd) into concentrated nitric acid (HNO_3), followed by evaporation and vacuum drying. The synthesis procedures for 4′-(4-carboxymethyl eneoxyphenyl)-2,2′:6′,2″-terpyridine (L-COOH) are in the ESI.† All the other starting materials and reagents were purchased from Sinopharm Chemical Reagent Corporation (China) and directly used without further purification.

Synthesis procedures

Synthesis of TTA-Si modified mesoporous silica nanoparticles (TTA-MSN). The modified precursor TTA-Si was synthesized *via* the reaction between TTA and TEPIC in THF as previously described.[28] The TTA-MSN particle, in which the organic ligand TTA was covalently grafted to the inorganic mesoporous silica matrix, was prepared by co-hydrolysis and co-condensation procedures using TTA-Si and TEOS as the silica source according to our previously reported method.[29] In a typical experimental procedure for TTA-MSN, a mixed solution was prepared by dissolving P123 (1.0 g) in a mixture of deionized water (7.5 g) and 2 M HCl solution (30 g) at 35 °C in a flask reactor. Then, a TEOS and TTA-Si mixture was added to the solution in the ratio TEOS : 0.04 NTA-Si : 0.0172 P123 : 6 HCl : 208.33 H_2O. The mixture was stirred for 24 h at 35 °C, and the as-synthesized suspension was transferred to a Teflon bottle, which was sealed in an autoclave and heated at 100 °C for 48 h. After the suspension was cooled to room temperature, the solid product was collected by filtration, washed thoroughly with deionized water, and air-dried for 12 h at 65 °C. The template removal for all as-prepared TTA-MSN particles was performed through Soxhlet extraction using ethanol under reflux for 48 h. The sample was dried overnight at 65 °C under vacuum.

Synthesis of Eu complex functionalized mesoporous hybrid material (Eu(TTA-MSN)$_2$L). Eu(TTA-MSN)$_2$L was prepared by anchoring Eu^{3+} to TTA-MSN and the HL ligand to complete the coordination sphere of Eu^{3+}. In a typical process, TTA-MSN was dispersed in an amount of ethanol solution of Eu$(NO_3)_3{\cdot}6H_2O$ with a 1 : 2 molar ratio of Eu^{3+} : TTA-MSN under stirring. Then, a HL solution in ethanol (with a 1 : 1 molar ratio of Eu^{3+} : HL) was added to complete the coordination sphere of Eu^{3+}. The mixture was refluxed at 65 °C for 12 h, and the material was recovered by filtration and extensive washing with ethanol. The content of Eu^{3+} in the mesoporous hybrid material was determined using the coordination titration method, and the N content was confirmed by elemental analysis. For Eu(TTA-MSN)$_2$L, Eu was 4.33%, and N was 2.92%. Scheme 1 shows the detailed synthesis process and predicted structure of Eu(TTA-MSN)$_2$L.

Luminescence measurements. The luminescence properties were investigated in both the solid state and solutions at room temperature. The luminescence (excitation and emission) spectra were obtained by using a Hitachi F-7000 phosphorimeter with a 150 W xenon lamp as the excitation source. The luminescence decay times were recorded by an Edinburgh fluorescence spectrometer FLS920P with a mF920H pulsed xenon flash lamp. The absolute quantum yield was determined using an integrating sphere, which was coated on the inside with $BaSO_4$, which was provided by an Edinburgh FLS920 phosphorimeter. The excitation wavelength of the measured emission quantum yield was 369 nm.

The luminescence responses of mesoporous hybrid Eu(TTA-MSN)$_2$L toward the aqueous solution of various metal cations were investigated in their suspensions. The suspensions were prepared by dispersing Eu(TTA-MSN)$_2$L powder (3 mg) into 3 mL aqueous solutions containing different metal cations (1 mM). Then, the mixtures were subjected to luminescence measurements. The luminescence data were collected after 10 min.

 This journal is © The Royal Society of Chemistry 2019

Published on 05 June 2019. Downloaded by KEAN UNIVERSITY on 7/18/2019 2:41:27 AM.

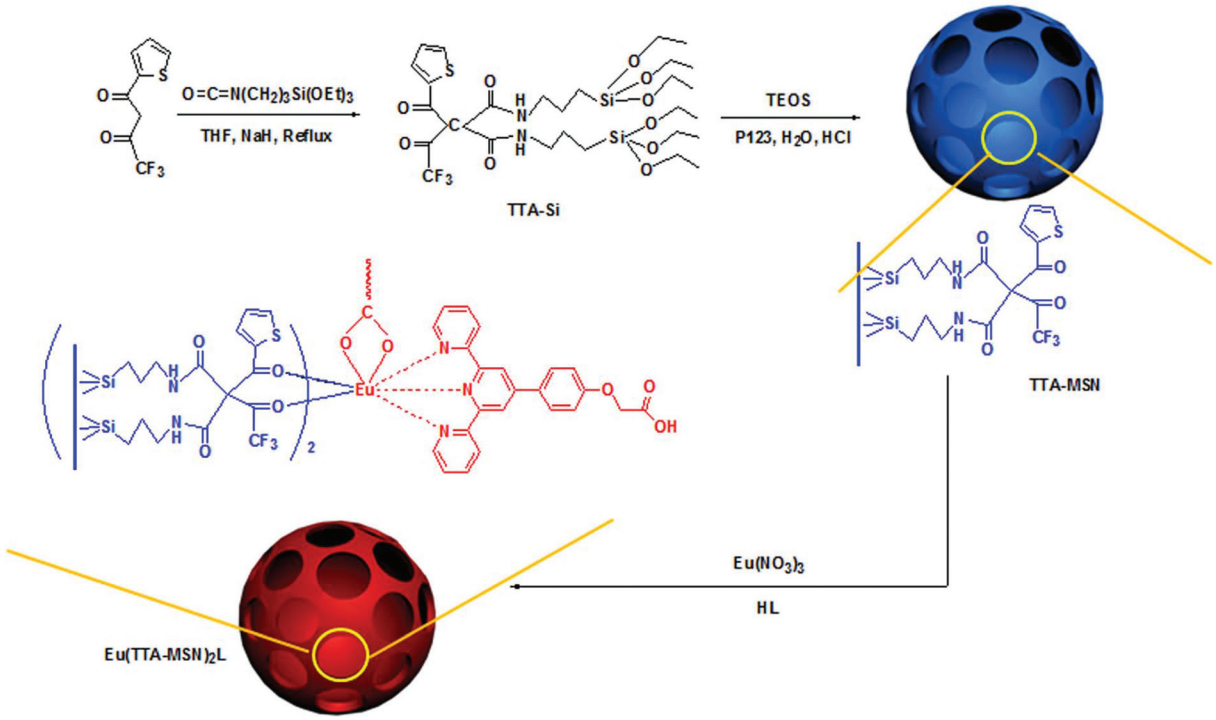

Scheme 1 Synthetic process and predicted structure of europium-containing mesoporous hybrid Eu(TTA-MSN)$_2$L.

Characterizations

The Fourier transform infrared (FTIR) spectra were obtained using the KBr pellet technique with a Nicolet 6700 spectrophotometer in the wavenumber range of 4000–400 cm^{-1}. The nuclear magnetic resonance (NMR) spectra were obtained using a Bruker AVANCE-500 spectrometer operating at 500 and 125 MHz for ^{1}H NMR and ^{13}C NMR spectroscopy, respectively. Elemental analysis (CHN) was performed with a Vario EL elemental analyzer, and the percentage of europium ions was obtained by EDTA titrimetric analysis. The room-temperature powder XRD data were collected with a Rigaku D/max2500VB+/PC diffractometer with Cu Kα (λ = 1.54 Å) radiation. Nitrogen adsorption–desorption isotherms were measured by using a Nova 2000 analyzer at liquid nitrogen temperature. The samples were measured after being vacuum-dried for 4 h at 120 °C. The surface areas were calculated by the Brunauer–Emmett–Teller (BET) method, and the pore size distributions were determined by the Barrett–Joyner–Halenda (BJH) method. High-resolution transmission electron microscopy (HRTEM) was performed with a JEOL JEM2011 electron microscope operated at 200 kV. The scanning electronic microscopy (SEM) images were captured by a HITACHI S-4200 field emission microscope. Thermogravimetric analysis (TGA) was conducted with a NETZSCH STA 449 F3 instrument up to 800 °C at a heating rate of 10 K min^{-1} under N_2.

Results and discussion

In this paper, a novel Eu complex functionalized SBA-15 mesoporous hybrid material Eu(TTA-MSN)$_2$L was designed and synthesized. First, di-silylated β-diketonate ligands (TTA-Si, TTA: 2-thenoyltrifluoroacetone) were covalently grafted onto a mesoporous SBA-15 backbone *via in situ* co-hydrolysis and co-condensation reactions to form the mesoporous hybrid material TTA-MSN. 4′-(4-Carboxy-methyleneoxyphenyl)-2,2′:6′,2″-terpyridinel (HL) was synthesized and used as the second ligand, whose three pyridine N atoms and carboxylate group can coordinate with Eu^{3+} ions and sensitize its luminescence. Finally, a material displaying orderly mesoporous structures, excellent luminescence property, and selective identification of Zn^{2+} ions was obtained through the coordination reaction between the rare-earth Eu ions and the two ligands (TTA-MSN and L$^-$). The fluorescent emission color of the Eu(TTA-MSN)$_2$L aqueous solution varied with the increase in Zn^{2+} concentration. Thus, we achieved a multicolor modulation that covered nearly the entire visible light region (including white-light emission) by simply controlling the Zn^{2+} concentration. This study offers a new strategy for tuning the full-color emission, including white-light emission.

Scheme 1 shows the detailed process and predicted structure of the mesoporous hybrid material Eu(TTA-MSN)$_2$L. A sol–gel reaction cannot be guaranteed in the synthesis process. As such, the exact composition is difficult to determine in this complex hybrid system. However, unlike the C or H elements, the contents of Eu^{3+} and N are constant and therefore cannot be changed by differences in the sol–gel process. Therefore, the molar ratios of Eu^{3+} and N can be used to predict the main composition of the mesoporous hybrids, especially the coordination environment surrounding Eu^{3+}. By considering the contents of Eu^{3+} and N, the molar ratio of Eu^{3+} and N can be cal-

Published on 05 June 2019. Downloaded by KEAN UNIVERSITY on 7/18/2019 2:41:27 AM.

culated as 1 : 7. Out of the seven N atoms, four were from two TTA-MSN units, and the other three were from one L unit, such that the ratio can demonstrate the composition of the mesoporous hybrid system. The coordination behavior could be predicted based on lanthanide chemistry principles and the properties of the functional group in the hybrid system. The central Eu^{3+} ion should be coordinated by four oxygen atoms from two chelating carbonyl groups of two TTA-MSN units, three pyridine N atoms from one organic ligand L, and two carboxyl oxygen atoms from another organic ligand L to form an eight-coordinated environment. This coordination behavior is easy to understand, because lanthanide complexes are most stable with a coordination number of 8 or 9. The coordination behavior of TTA-MSN and the organic ligand L is also well known.

Characterization of Eu(TTA-MSN)$_2$L

The FTIR spectra of TTA (A), TTA-Si (B), and TTA-Si modified mesoporous silica nanoparticles TTA-MSN (C) were compared to confirm whether the precursor and mesoporous hybrid material were successfully synthesized. The main absorptions and assignments are presented in Fig. S1.† All of the obtained data agreed with previously reported results. The FTIR spectra of organic ligand HL (A), pure SBA-15 (B), and Eu(TTA-MSN)$_2$L (C) are presented in Fig. 1. As shown in Fig. 1(A), we can observe that the evident peak at 1732 cm^{-1} was ascribed to the C═O stretching vibration, and the peak at 1468 cm^{-1} was attributed to the –OH bending vibration. As shown in Fig. 1(B), the evident peak at 1076 cm^{-1} resulted from the asymmetric Si–O stretching vibration modes, and the peak at 806 cm^{-1} was attributed to the symmetric Si–O stretching vibration. A Si–O–Si bending vibration was observed at 462 cm^{-1}, and the peak at 960 cm^{-1} was ascribed to the silanol (Si–OH) stretching vibrations of the surface groups. The peak at 3441 cm^{-1} confirmed the presence of a hydroxyl group. Compared with pure SBA-15, Eu(TTA-MSN)$_2$L exhibited similar infrared absorption bands to the silica framework. The absence of any strong peaks near 1732 cm^{-1} suggested that the carboxyl group of the ligand L^- in the hybrid material Eu(TTA-MSN)$_2$L was completely deprotonated.[30,31] The peaks located at 1603 and 1430 cm^{-1} were attributed to asymmetric and symmetric stretching vibrations of the COO^- groups, respectively. The separation between the ν_{as}(COO) and ν_s(COO) peaks was smaller than 200 cm^{-1}, confirming the didentate coordination mode of the carboxylate groups in Eu(TTA-MSN)$_2$L.[32] The peaks at 1641 and 1479 cm^{-1} were ascribed to the typical C═C and C═N stretching vibrations of pyridyl and benzene groups. Furthermore, the weak absorption band located at 2941 cm^{-1} was assigned to the methylene groups of TTA-MSN. These data suggested that the organic ligands (TTA-MSN and L^-) successfully coordinated with Eu^{3+}, and that a mesoporous hybrid material Eu(TTA-MSN)$_2$L was formed.

To confirm the hexagonal mesostructures, the small-angle X-ray diffraction patterns of TTA-Si modified mesoporous silica nanoparticles TTA-MSN and Eu(TTA-MSN)$_2$L are shown in Fig. 2. Both samples showed XRD patterns with three distinct reflections, namely, one intense peak and two weak reflections, which can be indexed as the (100), (110), and (200) planes related to a 2D (*P6mm*) pore array of SBA-15.[33,34] The values of the corresponding unit cell parameters a_0 ($a_0 = 2\ d_{100}/\sqrt{3}$) of TTA-MSN and Eu(TTA-MSN)$_2$L were 12.09 and 11.79, respectively. Compared with the XRD pattern of the TTA-MSN, the d_{100} spacing values of Eu(TTA-MSN)$_2$L were almost unchanged, indicating that the hexagonal ordering framework was retained after the Eu complex was introduced. Eu(TTA-MSN)$_2$L displayed a lower diffraction peak intensity than TTA-MSN, which is assigned to the immobilization of the Eu complex in the channels of SBA-15.

The characterization of N_2 adsorption–desorption for the mesoporous silica nanoparticles TTA-MSN and Eu complex functionalized mesoporous hybrid material Eu(TTA-MSN)$_2$L provides further proof of the preservation of the mesoporous structure after introduction of the Eu^{3+} ion. As shown in Fig. 3, both exhibited type-IV isotherms with H1-type hysteresis loops

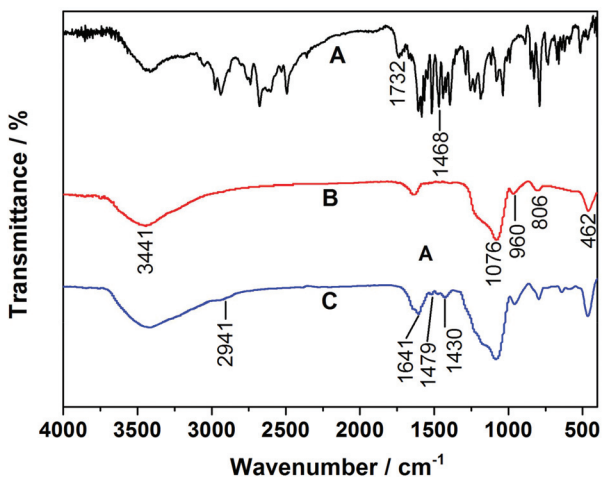

Fig. 1 FTIR spectra of organic ligand HL (A), pure SBA-15 (B), and Eu(TTA-MSN)$_2$L (C).

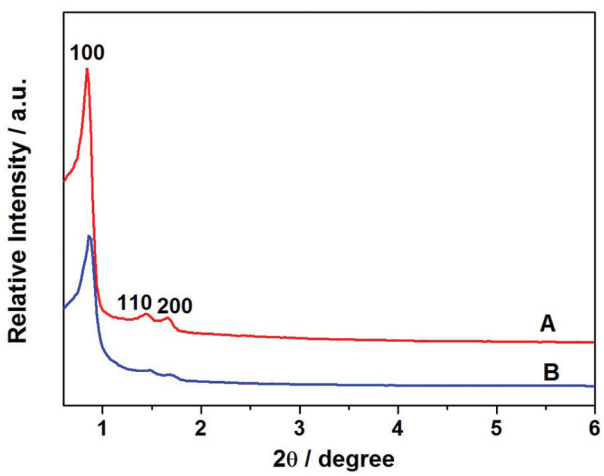

Fig. 2 Small-angle XRD patterns of TTA-MSN (A) and Eu(TTA-MSN)$_2$L (B).

This journal is © The Royal Society of Chemistry 2019

Published on 05 June 2019. Downloaded by KEAN UNIVERSITY on 7/18/2019 2:41:27 AM.

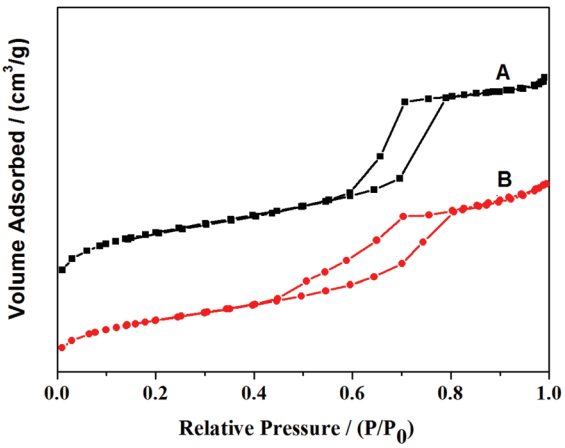

Fig. 3 N_2 adsorption–desorption isotherms for TTA-MSN (A) and Eu(TTA-MSN)$_2$L (B).

at high relative pressures according to the IUPAC classification.[35] Such a structure is characteristic of ordered mesoporous materials with highly uniform size distributions. The specific area and pore size were calculated using BET and BJH methods, respectively. Table 1 summarizes the structural data (BET surface area, total pore volume, pore size, *etc.*) of both mesoporous materials. Compared with TTA-MSN, Eu(TTA-MSN)$_2$L possessed a smaller surface area and a slightly smaller pore size and pore volume, mainly because europium complexes were grafted on the internal surface of the mesoporous silica SBA-15.[36] Furthermore, the grafted europium complexes did not destroy the mesoporous structure, which is consistent with the small-angle XRD results.

The high-resolution TEM images of Eu(TTA-MSN)$_2$L are presented in Fig. 4, which shows the typical hexagonal SBA-15 structure with homogeneous and ordered pores, suggesting that the ordered mesostructure of Eu(TTA-MSN)$_2$L was substantially conserved after the complexation process, which was consistent with the small-angle XRD and N_2 adsorption–desorption isotherms. The distance between the centers of the mesopore was estimated to be approximately 10 nm, which was consistent with the values calculated from the corresponding small-angle XRD analysis (Table 1).

Luminescence properties of Eu(TTA-MSN)$_2$L

The solid-state luminescence behavior of Eu(TTA-MSN)$_2$L was investigated at room temperature. The photoluminescence excitation and emission spectra of Eu(TTA-MSN)$_2$L are presented in Fig. S2† and Fig. 5, respectively. The excitation spectrum was obtained in the range of 200–500 nm at an emission wavelength of 616 nm. As presented in Fig. S2,† the excitation spectrum presented a broad band covering form 250 nm to 450 nm that was imposed with a weak peak centered at 394 nm. The prominent broad band was attributed to the $\pi \rightarrow \pi^*$ electron transition of the organic ligand HL, whereas the weak absorption band was ascribed to the f–f transition of Eu^{3+} ions. The emission spectrum of Eu(TTA-MSN)$_2$L, which was obtained at an excitation wavelength of 369 nm, presented five characteristic peaks at 579, 593, 616, 650, and 698 nm in the range of 550–750 nm. These peaks were associated with the 4f–4f transitions of the $^5D_0$ excited state to the low-lying ^7F_J (J = 1, 2, 3, 4, and 5) levels of Eu^{3+} ions. The hypersensitive transitions ($^5D_0 \rightarrow {}^7F_2$) at 616 nm dominated the entire emission spectra, resulting in the characteristic red luminescence of the europium mesoporous hybrid. The emissions of Eu^{3+} ions are generally used as a sensitive probe to investigate the local environment surrounding cations. The emission intensity of the electric dipole transition of $^5D_0 \rightarrow {}^7F_2$ at 616 nm was considerably higher than the orange emission intensities of the magnetic

Table 1 Structural parameters of TTA-MSN and Eu(TTA-MSN)$_2$L[a]

Sample	d_{100} (nm)	a_0 (nm)	S_{BET} ($m^2\ g^{-1}$)	V ($cm^3\ g^{-1}$)	D (nm)	t (nm)
TTA-MSN	10.47	12.09	726	0.81	6.34	5.75
Eu(TTA-MSN)$_2$L	10.21	11.79	586	0.59	5.58	6.21

[a] d_{100} is the d(100) spacing, a_0 the cell parameter ($a_0 = 2\ d_{100}/\sqrt{3}$), S_{BET} the BET surface area, V the total pore volume, D_{BJH} the average pore diameter, and t the wall thickness, calculated by $a_0 - D$.

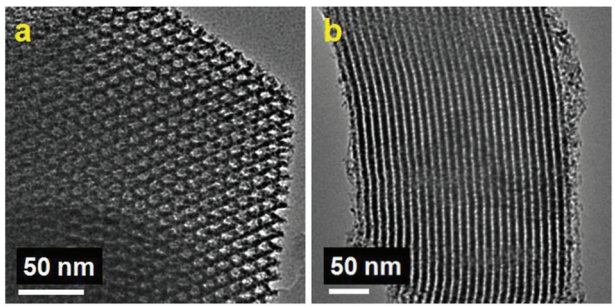

Fig. 4 High-resolution TEM images of Eu(TTA-MSN)$_2$L imaged along the [110] zone axis (a) and the [100] zone axis (b), respectively.

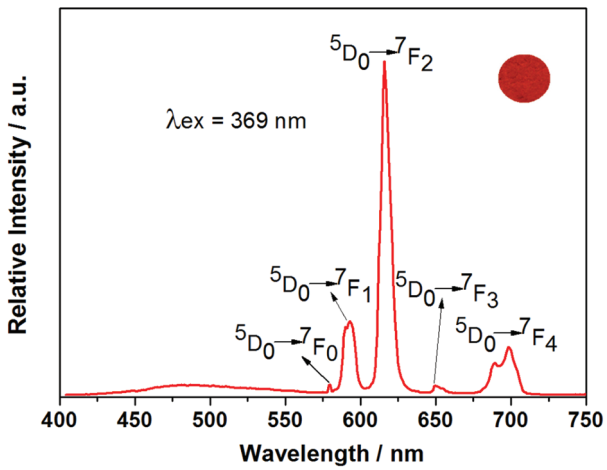

Fig. 5 Emission spectra of Eu(TTA-MSN)$_2$L. The inset shows the corresponding luminescence image under UV-light irradiation of 365 nm.

Published on 05 June 2019. Downloaded by KEAN UNIVERSITY on 7/18/2019 2:41:27 AM.

dipole transition of 593 nm, indicating that the europium ions were in an environment without an inversion symmetry.

The luminescence lifetime decay curves and luminescence quantum efficiency of Eu(TTA-MSN)$_2$L were measured to further investigate the luminescence properties. The mesoporous hybrid Eu(TTA-MSN)$_2$L presented reasonably long lifetimes (0.62 ms) and high quantum yields (18.4%), which were ascribed to the effective energy transfer from the ligands (TTA-MSN and L) to the central Eu^{3+} ions. The luminescence time decay curves for Eu(TTA-MSN)$_2$L are given in Fig. S3.† The results implied that mesoporous silica nanoparticles (SBA-15) can serve as an efficient host for sensitizing the luminescence of Eu^{3+} ions.

In addition, the luminescence properties of Eu(TTA-MSN)$_2$L in aqueous solution were investigated. As shown in Fig. S4,† the mesoporous hybrid material Eu(TTA-MSN)$_2$L in aqueous solution also exhibited five characteristic emission peaks of europium ions. Moreover, the Eu(TTA-MSN)$_2$L in aqueous solution displayed an excellent fluorescence stability at room temperature. The luminescence intensity of Eu(TTA-MSN)$_2$L in aqueous solution showed a limited reduction as the time progresses (Fig. S5†). The excellent luminescence property in aqueous solution, good stability, and the nanoscale nature of Eu(TTA-MSN)$_2$L make it very suitable for generating new florescence sensors in environmental and biological systems.

Sensing of Zn^{2+} cations

To examine the potential of Eu(TTA-MSN)$_2$L for the sensing of metal ions, the as-synthesized samples were immersed in aqueous solutions containing different metal ions (Zn^{2+}, Cd^{2+}, Cu^{2+}, Fe^{3+}, Mn^{2+}, Mg^{2+}, Ni^{2+}, Ca^{2+}, Na^{+}, K^{+}, Cr^{3+}, Co^{3+}, Ag^{+}, Pb^{2+}, and Hg^{2+}). The luminescence properties are recorded and compared in Fig. 6a. The results indicated that most of these cations, namely, Cd^{2+}, Cu^{2+}, Fe^{3+}, Mn^{2+}, Mg^{2+}, Ni^{2+}, Ca^{2+}, Na^{+}, K^{+}, Cr^{3+}, Co^{3+}, Ag^{+}, Pb^{2+}, and Hg^{2+}, slightly influenced the emission intensities of the mesoporous hybrid material, and they still showed the characteristic emission of Eu^{3+} ions. In addition, no changes in luminescent color were observed. However, only Zn^{2+} significantly affected the emission spectrum of Eu(TTA-MSN)$_2$L, and an obvious luminescent color change (from red to green) was easily observed with the naked eye under UV-light irradiation (Fig. 6b). The reason for the selective recognition of Eu(TTA-MSN)$_2$L toward Zn^{2+} may be that there existed stronger coordination interaction between L ligands and Zn^{2+} than L ligands and Eu^{3+}.[37]

Furthermore, the interference of other cations on the detection of Zn^{2+} was also determined. As shown in Fig. S6,† the emission intensity of the Eu mesoporous hybrid only exhibits slight changes in the presence of other cations. Upon introduction of Zn^{2+} into the mixture of the Eu mesoporous hybrid and other cations, an obvious fluorescence spectra change was observed. This result indicates that the interference caused by other cations can be neglected, further demonstrating that the Eu mesoporous hybrid sensor can efficiently recognize and sense Zn^{2+}.

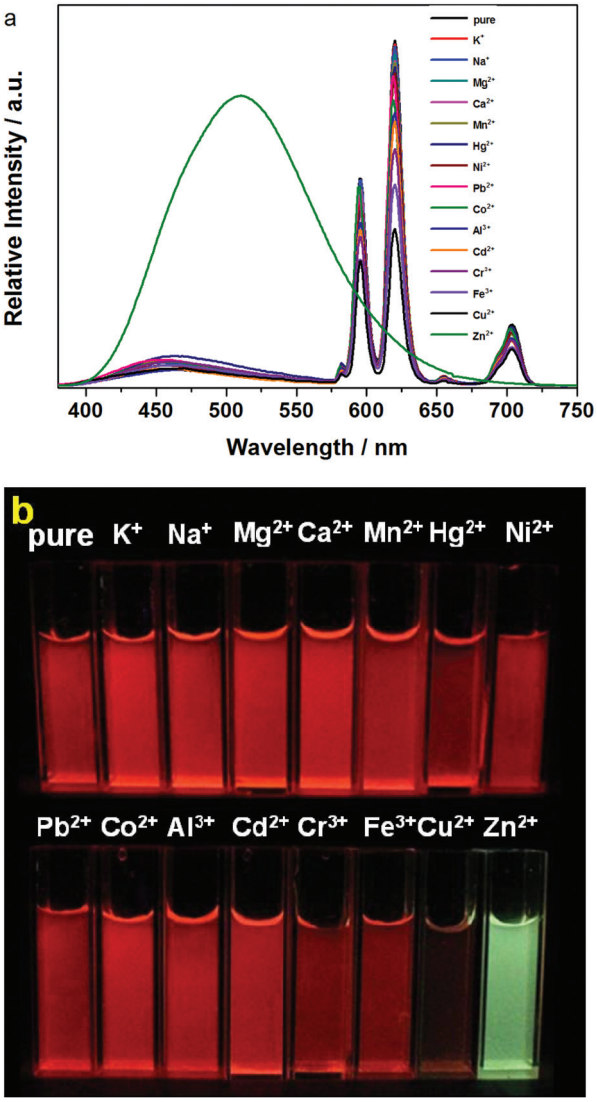

Fig. 6 (a) Emission spectra of Eu(TTA-MSN)$_2$L in the aqueous solutions containing different metal ions (1 mg mL^{-1}) when excited at 343 nm; (b) the corresponding luminescence image under UV-light irradiation of 365 nm.

To better understand the fluorescence response of Eu(TTA-MSN)$_2$L to Zn^{2+} cations, luminescence titration was conducted upon the addition of $Zn(NO_3)_2$ to Eu(TTA-MSN)$_2$L aqueous solution. As depicted in Fig. 7a, the emission intensity at 620 nm gradually declined, whereas the ligand-centered emission at 460 nm appeared, and its emission intensity gradually increased as the Zn^{2+} concentration increased from 0 mM to 0.06 mM. As the Zn^{2+} concentration further increased, the red emission from Eu^{3+} ions was almost completely quenched, and the ligand-centered emission red-shifted (from 460 nm to 510 nm), leading to an emission color change from red to green.

Changes in the fluorescent color of Eu(TTA-MSN)$_2$L aqueous solution in the presence of various concentrations of Zn^{2+} cations could be monitored by the naked eye under a por-

 This journal is © The Royal Society of Chemistry 2019

Published on 05 June 2019. Downloaded by KEAN UNIVERSITY on 7/18/2019 2:41:27 AM.

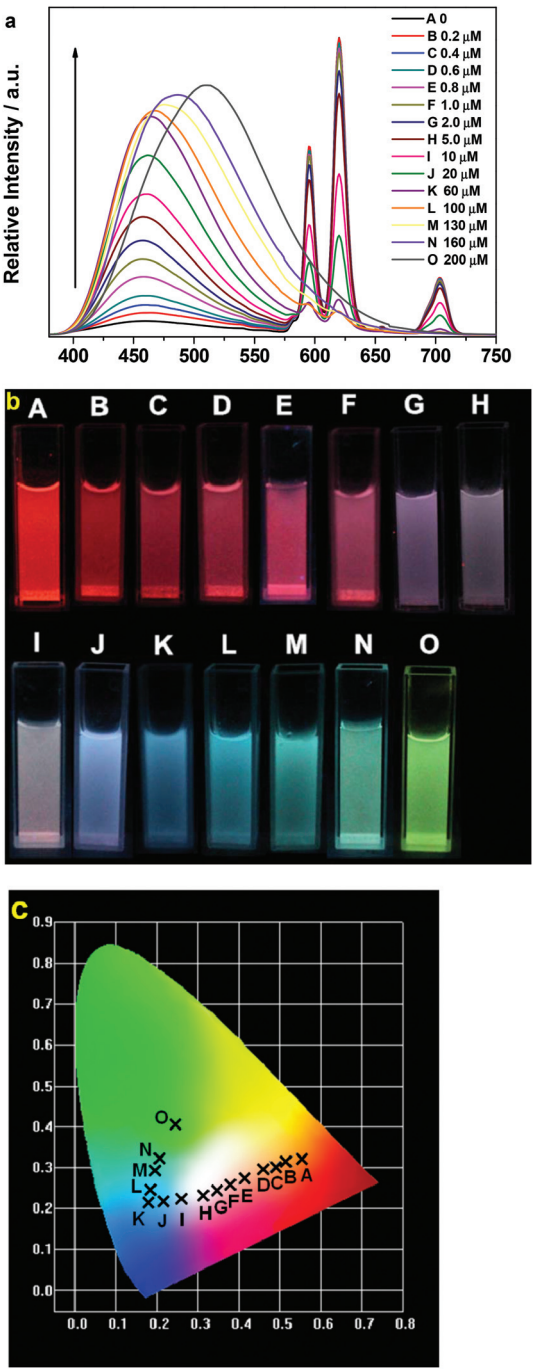

Fig. 7 (a) Photoluminescence spectra of Eu(TTA-MSN)$_2$L in aqueous solutions in the presence of various concentrations of Zn^{2+} at an excitation of 343 nm. (b) Changes in the fluorescent color of the corresponding solution under a hand-held UV lamp with an irradiation of 365 nm. (c) CIE chromaticity diagram showing the location of multicolor luminescence for A–O.

table UV lamp with an irradiation of 365 nm. Fig. 7b shows the fluorescence change of the Zn^{2+}-induced solution as the concentration of Zn^{2+} cations increased from 0 μM to 200 μM. With the increase of Zn^{2+} concentration, the solution fluorescence color gradually changed from red to pink, purplish pink, white, purplish blue, blue, greenish blue, bluish green, and finally green. The distinguishable colors at different Zn^{2+} concentrations were due to the rate of countercurrent fluorescence changes in the fluorescence emission band derived from ligand-centered emission and the characteristic emission of the Eu^{3+} ions. Thus, the naked-eye quantification recognition of Zn^{2+} cations is feasible through the color change of the Eu(TTA-MSN)$_2$L solution.

Therefore, by varying the concentration of Zn^{2+} cations in Eu(TTA-MSN)$_2$L aqueous solution, we can precisely manipulate the relative emission intensities of these two constituent colors, resulting in a tunable overall color output. The emission color coordinates (x, y) for Eu(TTA-MSN)$_2$L in aqueous solutions in the presence of various concentrations of Zn^{2+} excited at 343 nm in the CIE 1931 chromaticity diagram are shown in Fig. 7c and summarized in Table 2. It is worth noting that the white emission can be obtained when the Zn^{2+} concentration locates in the range of 5.0–10 μmol L^{-1}, which can be regarded as the result of comparative intensities of the blue and reddish orange emission. These findings open the possibility for many applications, such as single-phased white-emitting phosphors.

Fig. 8 shows the typical variations in the emission intensity ratio of 460 nm/620 nm as a function of the concentration of Zn^{2+}. When plotting the fluorescence intensity ratio *versus* the Zn^{2+} concentration in the range of 0–10^{-4} M, we observed that the calibration region followed the simple linear equation of $y = 0.0896 + 0.0941x$ by the least-squares fitting method, and the correlation coefficient $R^2 = 0.9983$. The limit of detection (LOD) for Zn^{2+} was determined as 9.2×10^{-5} M according to the equation LOD = 3SD per slope, indicating that Eu(TTA-MSN)$_2$L can be used as a highly sensitive probe for the quantitative luminescence detection of Zn^{2+} ions in aqueous media.

The possible sensing mechanism for the luminescence response to Zn^{2+} ions was further investigated. The luminescence emission changes of lanthanide complexes by metal cations originated from two aspects: the interaction between

Table 2 CIE coordinates and emission colors of A–O

Number	Zn^{2+} concentration (μmol L^{-1})	CIE (x, y)	Color
A	0	(0.55, 0.32)	Red
B	0.2	(0.52, 0.31)	Red
C	0.4	(0.49, 0.30)	Pink
D	0.6	(0.46, 0.30)	Pink
E	0.8	(0.41, 0.27)	Purplish pink
F	1.0	(0.38, 0.26)	Purplish pink
G	2.0	(0.35, 0.24)	Purplish pink
H	5.0	(0.31, 0.23)	White
I	10	(0.26, 0.22)	White
J	20	(0.22, 0.22)	Purplish blue
K	60	(0.18, 0.22)	Blue
L	100	(0.18, 0.25)	Greenish blue
M	130	(0.20, 0.29)	Bluish green
N	160	(0.21, 0.32)	Bluish green
O	200	(024, 0.40)	Green

Published on 05 June 2019. Downloaded by KEAN UNIVERSITY on 7/18/2019 2:41:27 AM.

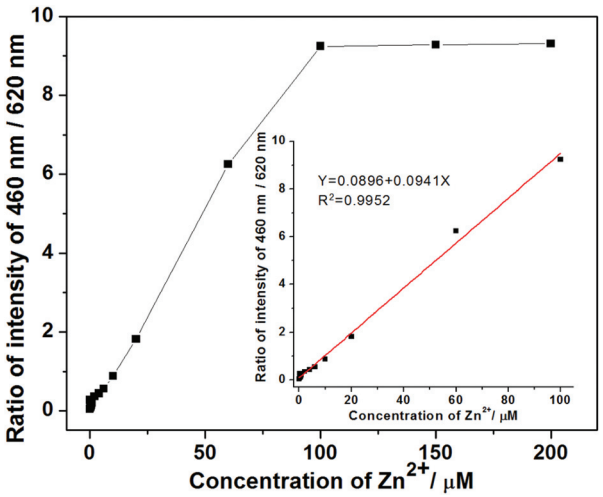
Ratio of intensity of 460 nm / 620 nm
Concentration of Zn2+/ μM
Y=0.0896+0.0941X
R²=0.9952
Ratio of intensity of 460 nm / 620 nm
Concentration of Zn2+/ μM

Fig. 8 Ratio of intensity of 460 nm/620 nm of Eu(TTA-MSN)$_2$L in aqueous solutions in the presence of various concentrations of Zn^{2+} at an excitation of 343 nm.

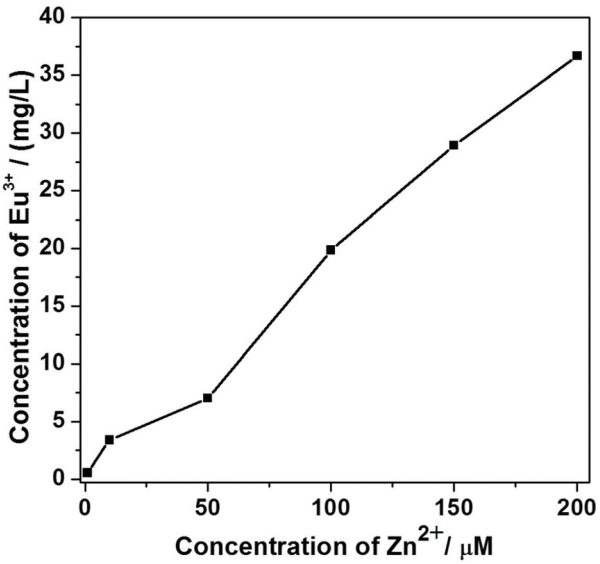

Fig. 9 Eu^{3+} concentrations of the filtrate solution of Eu(TTA-MSN)$_2$L upon the addition of different contents of Zn^{2+} ions.

metal cations and organic ligands;[38–40] and the cation exchange of central lanthanide ions in the lanthanide complexes with targeted cations.[41–43] Non-free coordination sites could bind to Zn^{2+} ions in Eu(TTA-MSN)$_2$L according to the predicted coordination composition of Eu(TTA-MSN)$_2$L. Therefore, we speculated that the luminescence emission changes of Eu(TTA-MSN)$_2$L by Zn^{2+} ions resulted from the cation exchange of Eu^{3+} in the parent material Eu(TTA-MSN)$_2$L with Zn^{2+}.

To verify this hypothesis, 5 mg of Eu(TTA-MSN)$_2$L was dispersed in 5 mL of Zn^{2+} solution at various concentrations. After immersing for 30 min, the filtrates were collected for ICP-MS measurements. Fig. 9 presents the Eu^{3+} concentration of the filtrate with different contents of added Zn^{2+}. The Eu^{3+} concentration of the filtrated solution gradually increased with the level of Zn^{2+}. Therefore, the Eu^{3+} ions in Eu(TTA-MSN)$_2$L were possibly replaced gradually by Zn^{2+} ions, which was consistent with the luminescence responses of Eu(TTA-MSN)$_2$L toward aqueous solutions of Zn^{2+} with various concentrations, implying that the luminescence emission changes resulted from the cation exchange.

The Zn^{2+} centered mesoporous hybrid Zn(TTA-MSN)L was obtained by dispersing Eu(TTA-MSN)$_2$L powder (3 mg) into 3 mL aqueous solutions containing Zn ions (1 mM). Similar to Eu(TTA-MSN)$_2$L, the exact structure and composition are difficult to determine in this kind of hybrid material because the synthesis process involves a sol–gel reaction that can't be guaranteed. However, we can predict the structure of the hybrid system Zn(TTA-MSN)L according to the Zn coordination chemistry principle and the configuration of the organic functional groups. Through the cation exchange, Zn^{2+} ions replaced Eu^{3+} ions in the mesoporous hybrid, and the coordination numbers of Zn^{2+} ions are usually 4 or 6, therefore we speculated that the Zn^{2+} ions are six coordinated, with three N atoms from L ligands, two O atoms from the TTA-MSN ligand, and one O atom from water molecules to form a six-coordinated environment. In addition, we obtained the emission spectra of the Zn-centered mesoporous hybrid Zn(TTA-MSN)L, as shown in Fig. S7.† Upon excitation at 343 nm, Zn(TTA-MSN)L exhibits a broad band centered at 498 nm, which was attributed to the ligand-to-metal-charge-transfer (LMCT).

Thermal stability of Eu(TTA-MSN)$_2$L

To investigate the thermal stability of Eu(TTA-MSN)$_2$L, TGA was conducted at a heating rate of 10 °C min^{-1} under a nitrogen atmosphere. The thermogravimetry analysis trace (TG) and differential thermogravimetry trace (DTG) curves of Eu(TTA-MSN)$_2$L are presented in Fig. 10. The TG curve showed that the decomposition of the hybrid Eu(TTA-MSN)$_2$L proceeded in three stages. The first weight loss of 3.9% below

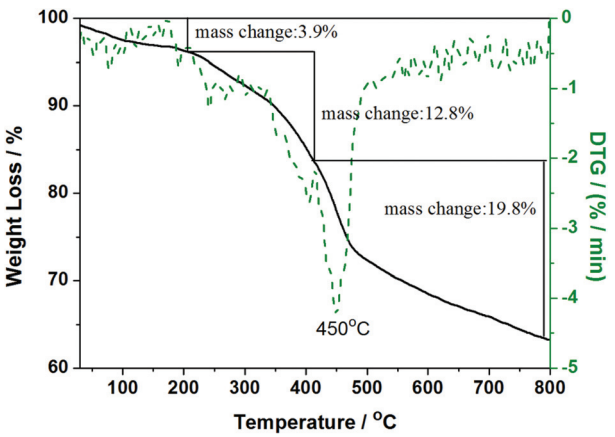

Fig. 10 Thermogravimetry analysis trace (TG) and differential thermogravimetry trace (DTG) curves of Eu complex functionalized mesoporous hybrid material Eu(TTA-MSN)$_2$L.

This journal is © The Royal Society of Chemistry 2019

Published on 05 June 2019. Downloaded by KEAN UNIVERSITY on 7/18/2019 2:41:27 AM.

207 °C was due to the physically adsorbed water and residual solvent without any decomposition of chemical bonds. The second weight loss (approximately 12.8%) occurred between 207 °C and 418 °C, which was ascribed to the decomposition of the incompletely removed surfactant. Finally, the weight loss (approximately 19.8%) that peaked at 450 °C corresponded to the collapse of the coordination structures and decomposition of the organic components. However, the pure complex began to lose considerable weight at 352 °C (Fig. S8†). This finding suggested that the thermal stability of the europium complex was enhanced as it covalently bonded with the SBA-15 mesoporous matrix.

Conclusions

In summary, a new Eu complex functionalized mesoporous hybrid material Eu(TTA-MSN)$_2$L was designed and synthesized as a highly selective and sensitive fluorescence sensor for the detection of Zn^{2+} ions in aqueous solution. This material retains its mesoscopically ordered structures and possesses good thermal stability and excellent luminescence properties (high color purity, long luminescence lifetime, and high quantum efficiency). Furthermore, the resultant mesoporous hybrid material exhibited multicolor emissions that depended on the concentration of Zn^{2+} ions in the water. The emitted color change of this sensor induced by Zn^{2+} ion concentration was distinguishable even with the naked eye under UV light irradiation of 365 nm. Therefore, this study provided a simple, effective, and visual fluorescent sensor that can detect Zn^{2+} ions in aqueous solutions. Moreover, a full-color emission, particularly white-light emission, could be also obtained by controlling the concentration of Zn^{2+} ions in Eu(TTA-MSN)$_2$L aqueous solution, thereby providing a new approach for achieving multi-color emitting materials.

Conflicts of interest

There are no conflicts to declare.

Acknowledgements

This work was financially supported by the National Natural Science Foundation of China (21771051 and 21401040), the Natural Science Foundation of Hebei Province (B2018208186 and B2018208112), the Hebei Province Department of Education Fund (QN2017072), the High-Level Talent Funding Project in Hebei (2016002014), and the Young Talent Support Plan of Hebei Province.

References

1 L. S. Yang, G. S. Li, M. L. Zhao, J. Zheng, D. Luo, Y. L. Zheng and L. P. Li, *Eur. J. Inorg. Chem.*, 2013, 5999–6008.
2 H. B. Wu, L. Ying, W. Yang and Y. Cao, *Chem. Soc. Rev.*, 2009, **38**, 3391–3400.
3 B. W. D'Andrade and S. R. Forrest, *Adv. Mater.*, 2004, **16**, 1585–1595.
4 S. Sivakumar, F. C. J. M. van Veggel and M. Raudsepp, *J. Am. Chem. Soc.*, 2005, **127**, 12464–12465.
5 J. W. Stouwdam, G. A. Hebbink, J. Huskens and F. C. van Veggel, *Chem. Mater.*, 2003, **15**, 4604–4616.
6 S. Y. Zhu and B. Yan, *New J. Chem.*, 2018, **42**, 4394–4401.
7 M. M. Shang, S. S. Liang, H. Z. Lian and J. Lin, *Inorg. Chem.*, 2017, **56**, 6131–6140.
8 P. K. Chen, Q. C. Li, S. Grindy and N. Holten-Andersen, *J. Am. Chem. Soc.*, 2015, **137**, 11590–11593.
9 G. G. Li, Z. Y. Hou, C. Peng, W. X. Wang, Z. Y. Cheng, C. X. Li, H. Z. Lian and J. Lin, *Adv. Funct. Mater.*, 2010, **20**, 3446–3456.
10 G. J. He, D. Guo, C. He, X. L. Zhang, X. W. Zhao and C. Y. Duan, *Angew. Chem., Int. Ed.*, 2009, **48**, 6132–6135.
11 Y. J. Cui, H. Xu, Y. F. Yue, Z. Y. Guo, J. C. Yu, Z. X. Chen, J. K. Gao, Y. Yang, G. D. Qian and B. L. Chen, *J. Am. Chem. Soc.*, 2012, **134**, 3979–3982.
12 S. Dang, J. H. Zhang and Z. M. Sun, *J. Mater. Chem.*, 2012, **22**, 8868–8873.
13 J. M. Berg and Y. Shi, *Science*, 1996, **271**, 1081–1085.
14 K. Hanaoka, K. Kikuchi, H. Kojima, Y. Urano and T. Nagano, *J. Am. Chem. Soc.*, 2004, **126**, 12470–12476.
15 T. V. Ohalloran, *Science*, 1993, **261**, 715–725.
16 T. Koike, T. Watanabe, S. Aoki, E. Kimura and M. Shiro, *J. Am. Chem. Soc.*, 1996, **118**, 12696–12703.
17 C. J. Frederickson, J. Y. Koh and A. I. Bush, *Nat. Rev. Neurosci.*, 2005, **6**, 449–462.
18 M. Roger, M. R. Figueroa, C. B. Azzeddine, V. Patinec, C. S. Bonnet, C. P. Iglesias and R. Tripier, *Eur. J. Inorg. Chem.*, 2014, **6**, 1072–1081.
19 T. Hirayama, M. Taki, K. Akaoka and Y. Yamamoto, *Bioorg. Med. Chem. Lett.*, 2012, **22**, 7410–7413.
20 K. Binnemans, *Chem. Rev.*, 2009, **109**, 4283–4374.
21 M. Fernandes, V. de Zea Bermudez, R. A. Sá Ferreira, L. D. Carlos, A. Charas, J. Morgado, M. M. Silva and M. J. Smith, *Chem. Mater.*, 2007, **19**, 3892–3901.
22 K. Binnemans and C. Görller-Walrand, *Chem. Rev.*, 2002, **102**, 2303–2345.
23 L. D. Carlos, R. A. S. Ferreira, V. de Zea Bermudez and S. J. L. Ribeiro, *Adv. Mater.*, 2009, **21**, 509–534.
24 O. Reany, T. Gunnlaugsson and D. Parker, *Chem. Commun.*, 2000, 473–474.
25 Z. Q. Ye, G. L. Wang, J. X. Chen, X. Y. Fu, W. Z. Zhang and J. L. Yuan, *Biosens. Bioelectron.*, 2010, **26**, 1043–1048.
26 J. B. Rivesta and P. K. Jain, *Chem. Soc. Rev.*, 2013, **42**, 89–96.
27 P. Wang, J. P. Ma, Y. B. Dong and R. Q. Huang, *J. Am. Chem. Soc.*, 2007, **129**, 10620–10621.
28 B. Yan and Y. Li, *Dalton Trans.*, 2010, **39**, 1480–1487.
29 Y. J. Li and B. Yan, *Inorg. Chem.*, 2009, **48**, 8276–8285.
30 Y. Q. Sun, J. Zhang, Z. F. Ju and G. Y. Yang, *Cryst. Growth Des.*, 2005, **5**, 1939–1943.

Published on 05 June 2019. Downloaded by KEAN UNIVERSITY on 7/18/2019 2:41:27 AM.

31 J. Xie, Q. R. Wu, H. M. Hu, Y. Cheng, M. L. Yang, F. X. Dong and G. L. Xue, *Polyhedron*, 2014, **83**, 92–101.
32 K. Nakamoto, *Infrared and Raman Spectra of Inorganic and Coordination Compounds, Part B*, John Wiley & Sons, Inc., New York, 5th edn, 1997.
33 K. S. W. Sing, D. H. Everett, R. A. W. Haul, L. Moscou, R. A. Pierotti, J. Rouquerol and T. Siemieniewska, *Pure Appl. Chem.*, 1985, **57**, 603–619.
34 M. Kruk and M. Jaroniec, *Chem. Mater.*, 2001, **13**, 3169–3183.
35 W. H. Zhang, X. B. Lu, J. H. Xiu, Z. L. Hua, L. X. Zhang, M. Robertson, J. L. Shi, D. S. Yan and J. D. Holmes, *Adv. Funct. Mater.*, 2004, **14**, 544–552.
36 C. Y. Peng, H. J. Zhang, J. B. Yu, Q. G. Meng, L. S. Fu, H. R. Li, L. N. Sun and X. M. Guo, *J. Phys. Chem. B*, 2005, **109**, 15278–15287.
37 X. D. Yu, Z. Y. Wang, Y. J. Li, L. J. Geng, J. J. Ren and G. L. Feng, *Inorg. Chem.*, 2017, **56**, 7512–7518.
38 X. Z. Song, S. Y. Song, S. N. Zhao, Z. M. Hao, M. Zhu, X. Meng, L. L. Wu and H. J. Zhang, *Adv. Funct. Mater.*, 2014, **24**, 4034–4041.
39 G. F. Ji, J. J. Liu, X. C. Gao, W. Sun, J. Z. Wang, S. L. Zhao and Z. L. Liu, *J. Mater. Chem. A*, 2017, **5**, 10200–10205.
40 W. Yan, C. L. Zhang, S. G. Chen, L. J. Han and H. G. Zheng, *ACS Appl. Mater. Interfaces*, 2017, **9**, 1629–1634.
41 S. Dang, E. Ma, Z. M. Sun and H. J. Zhang, *J. Mater. Chem.*, 2012, **22**, 16920–16926.
42 G. W. Xu, Y. P. Wu, W. W. Dong, J. Zhao, X. Q. Wu, D. S. Li and Q. C. Zhang, *Small*, 2017, **13**, 1602996.
43 Z. C. Hu, B. J. Deibert and J. Li, *Chem. Soc. Rev.*, 2014, **43**, 5815–5840.

This journal is © The Royal Society of Chemistry 2019